Revealing the Complex Lithiation Pathways and Kinetics of Core-Shell NiO@CuO Electrode

Abstract

Nanostructured composite electrodes with multiple active phases offer extraordinary performance that can be harnessed in future batteries. However, it is difficult to disclose the complicated reaction pathways. In this work, NiO@CuO core-shell nanocomposites are prepared and used as anodes for lithium-ion batteries, with superior rate and stability performance compared with single-phase CuO and NiO. Using a combination of *in situ* and *ex situ* electron microscopy, a two-stage lithiation reaction pathway on NiO@CuO is identified, with CuO reduced to Cu_2O first and followed by the simultaneous reduction of both Cu_2O and NiO to metals, resolving the existing inconsistency in literature. Chemomechanical simulation further discloses the key role of the core-shell structure in high cycling stability of NiO@CuO, which decreases the probability of cracking during the discharge-charge process. This work provides new insights to explore lithiation mechanisms and kinetics in novel electrodes, which contribute to further development of various electrode materials.

Keywords: lithium ion batteries; nickel/copper oxides electrodes; *ex/in situ* electron microscopy; lithium pathways; reaction kinetics

Graphical abstract

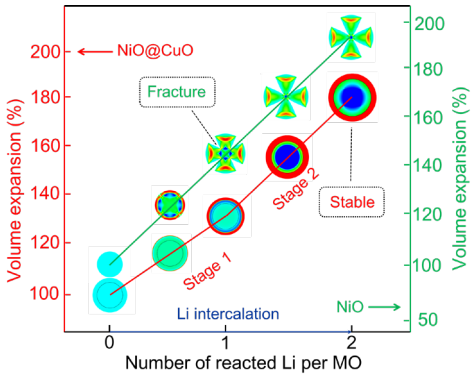

Three-dimensional core-shell structured NiO@CuO nanoparticles deliver high lithium storage performance. By incorporating advanced electron microscopic analysis with chemomechanical simulation, complex lithiation reaction pathways, the reaction kinetics and capacity contributions for different species are fully revealed.

1. Introduction

Metallic compounds such as oxides, chalcogenides, and phosphides[1-4] are highly promising electrode materials for their effective lithium ion storage with exceptionally large capacity. However, the discharge-charge mechanisms for these active materials can be quite complex, owing to their capability of both conversion and metallic alloying reactions with lithium ions, which gives rise to numerous possible reaction products.[5-8] Such mechanistic complexity is further exacerbated with the current trend of developing composite electrodes containing two or more active metal elements to gain much better performance than the single-component electrodes[9-12]. In particular, when two or more active materials form a heterostructure, benefits such as increased electron-transport channels, reduced ion-migration barriers, and mitigated volume change can be achieved from the synergistic interaction at the interface, promoting the electrode performance.[13-15] On the other hand, the competition between different active components in the heterostructured electrodes to react with lithium ions can complicate the reaction pathways, making it a challenge to identify the real discharge-charge mechanisms. As a typical example, the NiO-CuO composite electrodes with multiphases can exhibit high capacity and stability from the integration of the two active materials, but there still lacks of a consensus about their reaction pathways: Both the simultaneous reduction of NiO and CuO[16] and the separate reaction with CuO prior to NiO[17-19] have been reported, which makes the real discharge-charge mechanism ambiguous and debatable. Resolving such inconsistency is critical for the rational design and performance optimization of the electrode structure, and demands novel characterization strategies to perform systematic mechanistic studies.

In situ transmission electron microscopy (TEM) has been developed as a powerful tool to probe discharge-charge mechanisms in electrode materials through monitoring directly the structure and phase evolutions down to the atomic scale.[20-23] However, current *in situ* TEM studies on batteries are primarily limited to the open-cell configuration in vacuum, which uses alkali oxides as solid-state electrolytes to make contact with electrode materials and to perform discharge-charge cycling

through the contact point.[24-26] Despite numerous unprecedented mechanistic insights revealed by this setup, it is very different from a real battery with electrodes immersed in organic liquids, leading to the inevitable question of whether the obtained *in situ* observations faithfully reflect the true processes in a real battery.[27] Furthermore, the discharge-charge processes can be too fast for extended characterization such as spectroscopic mapping to track the evolution of local composition. Therefore, *in situ* TEM is mostly restricted to simple projection imaging and electron diffraction.[28, 29] It is also impractical to stop the processes in the middle of the *in situ* observation to do a more elaborated analysis on the potential intermediate phases.

Ex situ TEM on electrode materials extracted at various stages of the real battery operation, on the other hand, provides an alternative approach to interrogate discharge-charge mechanisms at nano or even atomic scale.[30, 31] Using the plateaus of the charge-discharge voltage profiles as an indicator, the intermediate reaction stages can be identified and suspended at the corresponding voltages. The reaction products can then be transferred to TEM for comprehensive analysis. The recent development of the identical-location strategy, using a conductive TEM grid to transfer the same batch of active materials between battery operation and TEM characterization, further enables sample tracking by ex situ TEM at various reaction stages.[31-34] Moreover, learning from the success of the biological cryo-EM, the liquid-nitrogen-cooling cryo-holder can also be incorporated in ex situ TEM to offer cryo-protection on the vulnerable active materials and solid-electrolyte interfaces (SEIs).[35-38] Nevertheless, as a post-mortem characterization, *ex situ* TEM is incapable of revealing detailed reaction kinetics of different stages. Accordingly, it is expected that ex situ and in situ TEM can be combined to offer complementary information on the reaction mechanisms.

In this work, we apply both *in situ* and *ex situ* TEM, facilitated by theoretical modeling, to unravel the complex reaction mechanism of NiO@CuO electrodes in Li-ion batteries (LIB). A unique NiO@CuO nanocomposite with CuO shells encompassing the hollow NiO cores is synthesized and achieves superior electrochemical performance than the single-phase CuO and NiO

nanoparticles. *Ex situ* TEM with the identical-location and cryo-protection strategies identifies unambiguously a two-stage lithiation pathway in such a heterostructural electrode, resolving the above-mentioned inconsistency in literature. *In situ* TEM further unveils the lithiation kinetics of the active materials, and demonstrates explicitly the instability instrinsic to NiO. Chemomechanical simulation coupling the diffusive reaction of Li with elasto-plastic deformation is established to theoretically investigate the lithiation-induced morphological changes in NiO and NiO@CuO particles, revealing that the excellent electrochemical stability in NiO@CuO can be attributed to the constraint of the stable CuO shell which maintains the integrity of the nanocomposite, and the special hollow structure to accommodate the large volume expansion of the NiO cores.

2. Results and discussion

The NiO@CuO core-shell nanocomposite supported on carbon nanotube (CNT) is synthesized via a phase-separation oxidation of impregnation-reduction generated NiCu alloy nanoparticles based on the Kirkendall effect.[39-41] As revealed by X-ray diffraction (XRD) in **Figure 1a**, NiCu alloy is oxidized to NiO (PDF#47-1049) and CuO (PDF#45-0937) phases after synthesis without showing any impurity. High-angle annular dark-field (HAADF) scanning TEM (STEM, **Figure 1b**) demonstrates the nanoparticle morphology of NiCu alloy, with smooth surface and homogeneously distributed Ni and Cu as unveiled by electron energy-loss spectroscopy (EELS) mapping in **Figure 1c**. After oxidation in air, the NiO@CuO core-shell nanocomposites are formed with an average size of ~129.3 nm (**Figure S1**) and the particles are much rougher on the surface (**Figure 1d, S2**). The relatively increased average particle size and rougher surface compared with the NiCu alloy particles are mainly ascribed to the outward migration tendency of metal species, which is non-uniform along different crystallographic directions at specific temperature in oxygen-rich atmosphere.[42] The core-shell hollow structure of NiO@CuO nanoparticles is unambiguously evinced by EELS elemental mapping and 3D electron tomography (**Figure 1e**, **Movie S1**). High-resolution TEM (HRTEM) further reveals phase separation inside the nanoparticles, with CuO (ICSD #9015924) shells outside

NiO (ICSD #1010095) cores as indicated by their lattice spacing labelled in **Figure 1f**. Besides, the selected area electron diffraction (SAED) pattern acquired on a randomly selected particle (**Figure 1g** and **Table S1**) also verifies the co-existence of CuO and NiO polycrystalline phases in one particle. For comparison, CuO and NiO nanoparticles supported on CNTs are also prepared by oxidizing Cu and Ni metals in air, respectively. Both samples show the hollow structure with high-quality polycrystalline structure similar to NiO@CuO, except that CuO has a much larger particle size of ~948.0 nm compared to that of NiO (~81.8 nm, **Figure S3, S4**). The oxidation states of Cu and Ni are also confirmed by X-ray photoelectron spectroscopy (XPS, **Figure 1h**). In particular, XPS shows much stronger CuO signals and very weak NiO signals from the NiO@CuO surface, further evidencing the structure of a NiO core coated by a CuO shell that has been revealed by TEM. The binding energy shifts of high-resolution Cu 2p and Ni 2p spectra compared to the monometal oxides also reflect the interaction between the NiO core and CuO shell.

The electrochemical performances of NiO@CuO/CNT, NiO/CNT, and CuO/CNT nanocomposites are measured in coin cells using Li foils as the counter/reference electrodes. As shown in the cyclic voltammogram (CV) in **Figure 2a**, the 1st cycle of CuO/CNT shows three distinct cathodic peaks at 1.2, 0.76, and 0.6 V, representing the reduction of CuO to Cu_2O, Cu_2O to Cu, and the formation of SEI, respectively.[43-45] Meanwhile, one anodic peak at 2.5 V corresponds to the oxidation of Cu to CuO. NiO/CNT presents only one broad cathodic and one anodic peak at 0.5 and 2.2 V, respectively, corresponding to the conversion between NiO and Ni phases. It is interesting that NiO@CuO/CNT also shows two prominent cathodic peaks at 1.2 and 0.6 V, clearly indicating a two-step reduction process similar to that of CuO/CNT. However, interpretation of the cathodic peaks in the NiO-CuO composite electrodes remains controversial, with both the simultaneous[16] and separate[17-19] reduction of CuO and NiO proposed in the literature. The single anodic peak for NiO@CuO/CNT at 2.2 V can be related to the oxidation of Ni/Cu to NiO/CuO.

The discharge-charge curves in the first five cycles (**Figure 2b**) demonstrate that

NiO@CuO/CNT exhibits much higher capacity, longer discharge platform, and slight improvement of initial Coulombic efficiency (56.3%) compared to that of CuO/CNT (39.8%) and NiO/CNT (51.4%). The rate capability of NiO@CuO/CNT is also outstanding and much higher than that of monoxide electrodes in capacitance, especially at high rates (**Figure 2c**). The long-term stability test demonstrates that NiO@CuO/CNT shows both excellent capacity and stability, retaining a 795 mAh g^{-1} capacity (91.4% retention) under 0.5 A g^{-1} after 1000 cycles (**Figure 2d**), whereas NiO/CNT decays quickly and CuO/CNT stays stable at a capacity of merely ~550 mAh g^{-1} for 200 cycles. According to the thermogravimetric analysis (TGA) results (**Figure S5**) and the specific capacity of CNT at 0.5 A g^{-1} reported in recent work,[46] the specific capacity provided by active materials are obtained as listed in **Table S2**. The electrodes running at 0.2 A g^{-1} shows the same tendency for 100 cycles (**Figure S6**), with the structure and morphology stability of NiO@CuO explicitly demonstrated by *ex situ* TEM shown in **Figure S7**. In addition, even under a high current density of 2 A g^{-1}, NiO@CuO/CNT can sustain a prolonged stable cyclic performance over 2000 cycles (**Figure S8**).

The electrochemical impedance spectroscopy (EIS, **Figure 2e** and **S9**) evinces smaller charge transfer resistance (R_{ct}) in NiO@CuO/CNT than that in CuO/CNT and NiO/CNT on both pristine and cycled electrodes (**Table S3**). The diffusion resistances (σ) calculated from the linearly fitted slopes (**Figure 2f** and **S10**, **Equation S1**) illustrate that the NiO@CuO/CNT electrode displays the smallest σ value of 49.6 $\Omega\ s^{-0.5}$ than NiO/CNT and CuO/CNT electrodes. The value of σ reduces with increasing cycle numbers. According to the relationship between σ and the diffusion coefficient of Li^+ (D_{Li+}, **Equation S2**), the histogram of D_{Li+} for different electrodes indicates faster Li^+ diffusion kinetics of NiO@CuO/CNT (**Figure 2g**). Moreover, CV measurements at different scan rates are performed and reveal the fast reaction kinetics of the NiO@CuO/CNT (**Figure S11**). The fast and surface controlled kinetics corroborate the high counter-ion mobility and ultra-fast electron transfer kinetics of the NiO@CuO/CNT electrode,[47] which can be ascribed to its unique structure, including

the hollow structure with interconnected pin holes, the coordination effect between Cu and Ni and the high electronic conductivity of surrounded carbon support.

To unravel the lithiation mechanism in NiO@CuO, we adopted *ex situ* TEM characterization incorporated with the *identical-location* strategy. The pre-characterized NiO@CuO nanoparticles are loaded onto a holey carbon-coated Cu TEM grid, which is further integrated into a coin cell to carry out discharge/charge measurements, as illustrated in **Figure 3a**.[48] Such a coin cell exhibits voltage profiles (**Figure 3b**) similar to the normal coin cells without TEM grids, which allows us to freeze the electrochemical reaction at the exact voltages corresponding to redox peaks of the CV profile (**Figure 2a**). The grid can then be extracted and transferred into TEM for nanoparticle tracking and structure comparison at the controlled discharge/charge states. To prevent beam damage on the active materials, *ex situ* TEM observation is performed at the cryogenic temperature (~98 K) using the liquid-nitrogen cooling holder, a proven strategy for LIB material characterization.[35-37, 49, 50] To minimize the potential effects of beam exposure on the lithiation behavior of NiO@CuO, we only carry out two (S)TEM observation on each tracked nanoparticle, i.e., one before and one after the coin cell measurement. Therefore, to derive the lithiation pathway with multiple steps, several nanoparticles need to be tracked to identify the structure evolution at different stages.

The pristine NiO@CuO particle characterized by EELS mapping (**Figure 3e**) shows typical NiO core and CuO shell similar to **Figure 1e**. Based on the CV testing and charge-discharge voltage profiles on NiO@CuO, three voltage cut-offs at 1.2, 0.5, and 0.05 V in the first discharge (lithiated state) and one at 2.4 V in the first charge (de-lithiated state) are chosen, as indicated in **Figure 3b**. The corresponding morphologies of the *ex situ* tracked nanoparticles are shown in the insets of **Figure 3b** (also see **Figure S12**), from which the volume expansion is measured and exhibits two typical stages at 0 to 2 h and 2 to 6 h during the discharge process (**Figure 3c**). *Ex situ* EELS mapping further reveals that, when NiO@CuO is discharged to 1.2 V, Li only reacts with the CuO shell, but the reduction of CuO is incomplete and forms Cu_2O (ICSD #9007497) as the reaction

product as identified consistently by HRTEM imaging (**Figure S13a**), selected area electron diffraction (SAED, **Figure 3d**), and EELS (**Figure 3f**). In particular, EELS reveals a chemical shift in the Cu L-edges[51] while no obvious change in the Ni L-edges (red lines, **Figure 3f**), indicating the coexistence of reduced Cu_2O and unreacted NiO phases at 1.2 V. The two characteristic peaks of the Li_2O phase at 59 and 63 eV start to appear,[52] whose exact positions are indicated by arrows. It demonstrates clearly that the 1.2 V cathodic peak in the CV measurement of NiO@CuO is solely due to the reduction of CuO to Cu_2O, which is in agreement with the previous report on the pure CuO electrodes.[53, 54]

When the NiO@CuO electrode is discharged to 0.5 V, it is observed in EELS maps that Li penetrates into the interior of the particle. Both metallic Cu (ICSD #9013014) and Ni (ICSD #9008476), as well as Li_2O (ICSD #1010064), are identified by HRTEM (**Figure S13b**) and SAED (**Figure 3d**). EEL spectra at 0.5 V (blue lines, **Figure 3f**) verify the reduction of NiO and Cu_2O to metallic Ni and Cu, evidenced by the lower L_3/L_2 ratio in the Ni L-edge[55, 56] and the step-like edge in the Cu L-edge.[51, 57] Furthermore, the Li_2O EELS signal becomes more prominent, suggesting the formation of more Li_2O. C K-edge shows the strong signal of C=O bond[48] (293 eV) after discharging, which indicates presumably the formation of SEIs from electrolyte decomposition. Therefore, the cathodic peak of NiO@CuO at 0.6 V should correspond to the simultaneous reduction of both Cu_2O and NiO to form metallic phases. It should be noted that no new phases are detected at voltage lower than 0.5 V (**Figure 3d** and **S13c**). We speculate that the capacity contribution at the potential range of 0.05 - 0.5 V is mainly attributed to the capacity of CNT. Our *ex situ* characterization thus unveils unequivocally the detailed two-step lithiation mechanism in NiO@CuO, with the reduction of CuO to Cu_2O first, followed by the simultaneous reduction of both Cu_2O and NiO to metals. The preferential reduction of CuO prior to NiO is consistent with their standard reduction potentials[58] and has also been proposed in literature based on CV measurements of NiO-CuO composites.[17-19] However, without the detailed microscopy studies, it was interpreted as a

complete separation between CuO and NiO reductions,[17-19] rather than the partially overlapped reduction as we have discovered in the present work.

When charging back to 2.4 V, EELS maps in **Figure 3e** show that most of Li is extracted from the NiO@CuO particle but presents a Li-rich surface, which probably reflects the SEI formed during the first discharge.[59] HRTEM and SAED verify the recovery of CuO and NiO phases at this voltage, while the broader SAED peaks in the intensity profile (**Figure 3d**) compared to the pristine state are owing to the formation of nanocrysalline CuO and NiO (inset schematic in **Figure 3d**, also see **Figure S13d**). Corresponding EEL spectra (**Figure 3f**) further reveals the coexistence of CuO and Cu_2O species, reflecting the in-progress charging reaction. Most of the tracked NiO@CuO particles survive during the first cycling with the core-shell structure largely maintained, demonstrating the structure stability that underpins the electrochemical cycling stability as shown in **Figure 2d**.

We further explore the lithiation kinetics in this system utilizing *in situ* TEM characterization. The *in situ* TEM holder setup is illustrated in **Figure 4a**, where one tungsten tip attached with metal oxide nanoparticles is used as the working electrode and the opposite tungsten tip with Li metal serves as the reference/counter electrode. The same -5 V voltage bias is applied between the two tips to better compare the lithiation behaviors of the three samples. As presented in **Figure 4b** and **Movie S2**, *In situ* TEM on NiO nanoparticles reveals dramatic expansion upon lithiation that eventually leads to the fracture of particles, explaining their poor cycling stability (**Figure 2d**). *In situ* SAED on the fractured NiO nanoparticle (**Figure 4d**) indicates a nearly complete reduction with all NiO transformed into Ni metal and Li_2O ($NiO + 2Li \rightarrow Ni + Li_2O$).

In situ TEM on NiO@CuO also displays the two-step lithiation process, which is consistent with both CV measurements and *ex situ* TEM characterization. As shown in **Figure 4c and Movie S3**, at the first stage (260 s), the CuO outer shell (red arrow) swells while the core of the nanoparticle changes little, agreeing with the preferential reduction of CuO to Cu_2O identified via *ex situ* TEM. The uniform contrast of the swelling shell can be attributed to the formation of nanocrystalline Cu_2O

and Li_2O with diminished diffraction contrast. At the second stage, the core of the nanoparticle starts to expand with the reduced diffraction contrast. The lithiation completes after ~760 s as indicated by *in situ* SAED (**Figure 4e**) and EELS (**Figure 4f**), both showing the full reduction of oxides into metallic Ni and Cu together with Li_2O. It is noted that *in situ* SAED and EELS present very similar results as *ex situ* TEM observation in **Figure 3**, validating that the *in situ* observation here can faithfully reflect the structural evolution in a real battery. More importantly, the NiO@CuO nanoparticle remains integrated with the core-shell structure preserved throughout the whole lithiation process, demonstrating its high structural stability that results in better cycling stability than that of NiO. Similar structure stability is also observed in CuO using *in situ* TEM lithiation ($CuO + 2Li \rightarrow Cu + Li_2O$) (**Figure S14-S16**, **Movie S4**).

Through a comparison of unit cell volumes of transition-metal and Li phases before and after lithiation reactions, the theoretical volume expansion for each reaction pathway can be derived as plotted in **Figure 5a**. By adopting the two-step lithiation identified by *ex situ* TEM and assuming Ni:Cu = 1:1.3 as derived from EELS mapping, the overall volume expansion of NiO@CuO is in between NiO and CuO, with NiO showing the largest expansion of ~191% (**Figure 5a**). *In situ* lithiation in TEM further allows us to quantitatively derive the volume expansion as a function of time, as summarized in **Figure 5c**. The overall volume expansions for NiO, CuO, and NiO@CuO are measured to be ~194%, 161%, and 176%, respectively, which are in remarkable agreement with theoretical calculations (**Figure 5a** and **b**). **Figure 5c** also reveals the two-stage expansion in both CuO and NiO@CuO: CuO shows a higher volume expansion rate first and then becomes slower, while NiO@CuO displays the opposite trend, both of which are properly predicted in **Figure 5a**. In distinct contrast, the very steep expansion curve of NiO indicates the ultrahigh expansion rate driven by the fast lithiation kinetics.

As the lithiation-induced large volume expansion always causes stress that subsequently leads to the failure of the materials, chemomechanical simulation is conducted herein to investigate the

morphological and stress evolutions in the NiO and NiO@CuO particles during lithiation. The simulated time-series snapshots of Li concentration and maximum principal stress distributions are shown in **Figure 5d** and **5e**, respectively. The corresponding movie (**Movie S5**) is provided in the Supporting Information. As displayed in **Figure 5d,** the red color indicates the fully lithiated phase (c = 1), while the blue represents the unlithiated phase (c = 0). The transition from blue to red stands for the intermediate phases. During lithiation, Li flows into the particle from the outer surface along the radial direction, with the reaction front identified by the sharp change of Li concentration (**Figure 5d**). As NiO possesses very fast lithiation kinetics, the rapid Li insertion generates high enough tensile stress in the lithiated outer shell, causing the fracture of the particle (**Figure 5e**). Even though the stress near the fractured region can get relaxed to some extent, the lithiation-induced stress concentration at crack tips can still drive the propagation of cracks, leading to the final failure of the particle. In contrast, the NiO@CuO particle experiences a much slower lithiation process than the NiO particle, with the outer CuO shell lithiated first and then the inner NiO core. Due to the constraint effect of the relatively strong CuO shell, the lithiation-induced volume expansion of the inner NiO core is highly suppressed, generating tensile stress (red) in the CuO shell while compression (blue) in the NiO core. Such regulated stress distribution can help to effectively mitigate the fracture behavior of the NiO core, contributing to the high cycling stability of NiO@CuO. Both the above simulated lithiation processes and the associated volume expansion (**Figure 5b**) are fully consistent with our *in situ* TEM observation.

3. Conclusions

In summary, the lithium storage mechanism of the core-shell nanostructured NiO@CuO nanocomposite has been revealed by combining *in situ*, *ex situ* TEM, and chemomechanical simulation. The unique NiO@CuO nanoparticles with CuO shells surrounding the hollow NiO cores are synthesized via the facile phase-separation strategy and exhibit excellent electrochemical behaviors, especially the superior rate performance and long-term stability. *Ex situ* TEM identifies a

two-stage lithiation pathway, in which the CuO shell is first reduced to cuprous oxide, and then followed by the simultaneous reduction of the residual oxides, resolving the existing inconsistency in literature. *In situ* TEM further unveils the lithiation kinetics of the active materials, and demonstrates explicitly the intrinsic instability of NiO. Moreover, chemomechanical simulation coupling the diffusion/reaction of Li with elasto-plastic deformation illustrates that the core-shell structure of NiO@CuO can effectively regulate stress distribution in the material, leading to the high electrochemical stability of NiO@CuO. The present study deepens our understanding of the lithiation mechanism and kinetics in the NiO/CuO-based multiphase electrodes. At last, the combination of *in situ* and *ex situ* analysis demonstrated in this work can be extended to other complex electrodes, offering a powerful tool to investigate intriguing charge-discharge mechanisms for novel electrode materials.

Acknowledgements

The authors are grateful for the support from xxx.

References

[1] P. Poizot, S. Laruelle, S. Grugeon, L. Dupont, J. Tarascon, Nano-sized transition-metal oxides as negative-electrode materials for lithium-ion batteries. Nature 407(2000) 496-499.

[2] M. Reddy, G. Subba Rao, B. Chowdari, Metal oxides and oxysalts as anode materials for Li ion batteries. Chem. Rev. 113(2013) 5364-5457.

[3] S. Fang, D. Bresser, S. Passerini, Transition metal oxide anodes for electrochemical energy storage in lithium-and sodium-ion batteries. Adv. Energy Mater. 10(2020) 1902485.

[4] Q. Li, H. Li, Q. Xia, Z. Hu, Y. Zhu, S. Yan, C. Ge, Q. Zhang, X. Wang, X. Shang, Extra storage capacity in transition metal oxide lithium-ion batteries revealed by *in situ* magnetometry. Nat. Mater. 20(2021) 76-83.

[5] W. Li, H. Li, Z. Lu, L. Gan, L. Ke, T. Zhai, H. Zhou, Layered phosphorus-like GeP_5: a promising anode candidate with high initial coulombic efficiency and large capacity for lithium ion batteries. Energy Environ. Sci. 8(2015) 3629-3636.

[6] S. Wang, P. Xiong, X. Guo, J. Zhang, X. Gao, F. Zhang, X. Tang, P. H. Notten, G. Wang, A stable conversion and alloying anode for potassium-ion batteries: a combined strategy of encapsulation and confinement. Adv. Funct. Mater. 30(2020) 2001588.

[7] X. Ou, C. Yang, X. Xiong, F. Zheng, Q. Pan, C. Jin, M. Liu, K. Huang, A new rGO-overcoated Sb_2Se_3 nanorods anode for Na^+ battery: *in situ* X-ray diffraction study on a live sodiation/desodiation process. Adv. Funct. Mater. 27(2017) 1606242.

[8] Q. Yun, L. Li, Z. Hu, Q. Lu, B. Chen, H. Zhang, Layered transition metal dichalcogenide-based nanomaterials for electrochemical energy storage. Adv. Mater. 32(2020) 1903826.

[9] W. Li, J. Liao, X. Li, L. Zhang, B. Zhao, Y. Chen, Y. Zhou, Z. Guo, M. Liu, $Zn(Cu)Si_{2+x}P_3$ solid solution anodes for high-performance Li-ion batteries with tunable working potentials. Adv. Funct. Mater. 29(2019) 1903638.

[10] B. Farbod, K. Cui, W. P. Kalisvaart, M. Kupsta, B. Zahiri, A. Kohandehghan, E. M. Lotfabad, Z.

Li, E. J. Luber, D. Mitlin, Anodes for sodium ion batteries based on tin-germanium-antimony alloys. ACS Nano 8(2014) 4415-4429.

[11] X. Ou, L. Cao, X. Liang, F. Zheng, H.-S. Zheng, X. Yang, J.-H. Wang, C. Yang, M. Liu, Fabrication of SnS_2/Mn_2SnS_4/carbon heterostructures for sodium-ion batteries with high initial coulombic efficiency and cycling stability. ACS Nano 13(2019) 3666-3676.

[12] Y. Zhao, X. Li, B. Yan, D. Xiong, D. Li, S. Lawes, X. Sun, Recent developments and understanding of novel mixed transition-metal oxides as anodes in lithium ion batteries. Adv. Energy Mater. 6(2016) 1502175.

[13] N. Zhao, J. Qin, L. Chu, L. Wang, D. Xu, X. Wang, H. Yang, J. Zhang, X. Li, Heterogeneous interface of Se@Sb@C boosting potassium storage. Nano Energy 78(2020) 105345.

[14] B. Chen, L. Yang, X. Bai, Q. Wu, M. Liang, Y. Wang, N. Zhao, C. Shi, B. Zhou, C. He, Heterostructure engineering of core-Shelled Sb@Sb_2O_3 encapsulated in 3D N-Doped carbon hollow-spheres for superior sodium/potassium storage. Small 17(2021) 2006824.

[15] W. Li, Q. Ma, P. Shen, Y. Zhou, L. Soule, Y. Li, Y. Wu, H. Zhang, M. Liu, Yolk-shell structured $CuSi_2P_3$@Graphene nanocomposite anode for long-life and high-rate lithium-ion batteries. Nano Energy 80(2021) 105506.

[16] L. Lefrançois Perreault, F. Colò, G. Meligrana, K. Kim, S. Fiorilli, F. Bella, J. R. Nair, C. Vitale-Brovarone, J. Florek, F. Kleitz, Spray-dried mesoporous mixed Cu-Ni oxide@graphene nanocomposite microspheres for high power and durable Li-ion battery anodes. Adv. Energy Mater. 8(2018) 1802438.

[17] W. Guo, W. Sun, Y. Wang, Multilayer CuO@NiO hollow spheres: microwave-assisted metal-organic-framework derivation and highly reversible structure-matched stepwise lithium storage. ACS Nano 9(2015) 11462-11471.

[18] Y.-W. Cheng, C.-H. Chen, S.-W. Yang, Y.-C. Li, B.-L. Peng, C.-C. Chang, R.-C. Wang, C.-P. Liu, Freestanding three-dimensional CuO/NiO Core-Shell nanowire arrays as high-performance

lithium-ion battery anode. Sci. Rep. 8(2018) 18034.

[19] H. Chen, C.-L. Li, N. Li, K.-X. Xiang, Z.-L. Hu, Facile synthesis of CuO–NiO nanocomposites with high surface areas and their application for lithium-ion batteries. Micro Nano Lett. 8(2013) 544-548.

[20] S. Hwang, X. Chen, G. Zhou, D. Su, *In situ* transmission electron microscopy on energy-related catalysis. Adv. Energy Mater. 10(2020) 1902105.

[21] C. Zhang, K. L. Firestein, J. F. Fernando, D. Siriwardena, J. E. von Treifeldt, D. Golberg, Recent progress of *in situ* transmission electron microscopy for energy materials. Adv. Mater. 32(2020) 1904094.

[22] H. Huang, J. Wang, X. Yang, R. Hu, J. Liu, L. Zhang, M. Zhu, Unveiling the advances of nanostructure design for alloy-type potassium-ion battery anodes via *in situ* TEM. Angew. Chem. Int. Ed. 132(2020) 14612-14618.

[23] X. Wu, S. Li, B. Yang, C. Wang, *In situ* transmission electron microscopy studies of electrochemical reaction mechanisms in rechargeable batteries. Electrochem. Energy Rev. 2(2019) 467-491.

[24] D. Liu, Z. Shadike, R. Lin, K. Qian, H. Li, K. Li, S. Wang, Q. Yu, M. Liu, S. Ganapathy, Review of recent development of *in situ*/operando characterization techniques for lithium battery research. Adv. Mater. 31(2019) 1806620.

[25] J. Cui, H. Zheng, K. He, *In situ* TEM study on conversion-type electrodes for rechargeable ion batteries. Adv. Mater. 33(2021) 2000699.

[26] C. Wang, L. Han, R. Zhang, H. Cheng, L. Mu, K. Kisslinger, P. Zou, Y. Ren, P. Cao, F. Lin, H. L. Xin, Resolving atomic-scale phase transformation and oxygen loss mechanism in ultrahigh-nickel layered cathodes for cobalt-free Lithium-ion batteries. Matter 4(2021) 2013-2026.

[27] Y. Yuan, K. Amine, J. Lu, R. Shahbazian-Yassar, Understanding materials challenges for rechargeable ion batteries with in situ transmission electron microscopy. Nat. Commun. 8(2017)

15806.

[28] Y. Fu, X. Guo, Z. Xu, G. Zhao, C. Xu, Y. Zhu, L. Zhou, Nanostructure-mediated phase evolution in lithiation/delithiation of Co_3O_4. ACS Appl. Mater. Interfaces 13(2021) 28171–28180.

[29] X. Du, X. Guo, J. Huang, Z. Lu, H. Tan, J.-Q. Huang, Y. Zhu, B. Zhang, Exploring the structure evolution of MoS_2 upon Li/Na/K ion insertion and the origin of the unusual stability in potassium ion batteries. Nanoscale Horiz. 5(2020) 1618-1627.

[30] R. Lin, E. Hu, M. Liu, Y. Wang, H. Cheng, J. Wu, J.-C. Zheng, Q. Wu, S. Bak, X. Tong, R. Zhang, W. Yang, K. A. Persson, X. Yu, X.-Q. Yang, H. L. Xin, Anomalous metal segregation in lithium-rich material provides design rules for stable cathode in lithium-ion battery. Nat. Commun. 10(2019) 1650.

[31] R. Lin, S.-M. Bak, Y. Shin, R. Zhang, C. Wang, K. Kisslinger, M. Ge, X. Huang, Z. Shadike, A. Pattammattel, H. Yan, Y. Chu, J. Wu, W. Yang, M. S. Whittingham, H. L. Xin, X.-Q. Yang, Hierarchical nickel valence gradient stabilizes high-nickel content layered cathode materials. Nat. Commun. 12(2021) 2350.

[32] N. Spinner, L. Zhang, W. E. Mustain, Investigation of metal oxide anode degradation in lithium-ion batteries via identical-location TEM. J. Mater. Chem. A 2(2014) 1627-1630.

[33] S.-Y. Lee, K.-Y. Park, W.-S. Kim, S. Yoon, S.-H. Hong, K. Kang, M. Kim, Unveiling origin of additional capacity of SnO_2 anode in lithium-ion batteries by realistic *ex situ* TEM analysis. Nano Energy 19(2016) 234-245.

[34] J. Huang, X. Guo, X. Du, X. Lin, J.-Q. Huang, H. Tan, Y. Zhu, B. Zhang, Nanostructures of solid electrolyte interphases and their consequences for microsized Sn anodes in sodium ion batteries. Energy Environ. Sci. 12(2019) 1550-1557.

[35] X. C. Ren, X. Q. Zhang, R. Xu, J. Q. Huang, Q. Zhang, Analyzing energy materials by cryogenic electron microscopy. Adv. Mater. 32(2020) e1908293.

[36] X. F. Wang, Y. J. Li, Y. S. Meng, Cryogenic electron microscopy for characterizing and

diagnosing batteries. Joule 2(2018) 2225-2234.

[37] M. J. Zachman, Z. Tu, S. Choudhury, L. A. Archer, L. F. Kourkoutis, Cryo-STEM mapping of solid-liquid interfaces and dendrites in lithium-metal batteries. Nature 560(2018) 345-349.

[38] J.-Q. Huang, X. Guo, J. Huang, H. Tan, X. Du, Y. Zhu, B. Zhang, Critical roles of microstructure and interphase on the stability of microsized germanium anode. J. Power Sources 481(2021) 228916.

[39] Y. Yin, R. M. Rioux, C. K. Erdonmez, S. Hughes, G. A. Somorjai, A. P. Alivisatos, Formation of hollow nanocrystals through the nanoscale Kirkendall effect. Science 304(2004) 711-714.

[40] W. Xia, Y. Yang, Q. Meng, Z. Deng, M. Gong, J. Wang, D. Wang, Y. Zhu, L. Sun, F. Xu, J. Li, H. L. Xin, Bimetallic nanoparticle oxidation in three dimensions by chemically sensitive electron tomography and in situ transmission electron microscopy. ACS Nano 12(2018) 7866-7874.

[41] J. Zhu, W. Tu, H. Pan, H. Zhang, B. Liu, Y. Cheng, Z. Deng, H. Zhang, Self-templating synthesis of hollow Co_3O_4 nanoparticles embedded in N, S-dual-doped reduced graphene oxide for lithium ion batteries. ACS Nano 14(2020) 5780-5787.

[42] L. Han, Q. Meng, D. Wang, Y. Zhu, J. Wang, X. Du, E.A. Stach, H. L. Xin, Interrogation of bimetallic particle oxidation in three dimensions at the nanoscale. Nat. Commun. *7*(2016) 13335.

[43] S. Jia, Y. Wang, X. Liu, S. Zhao, W. Zhao, Y. Huang, Z. Li, Z. Lin, Hierarchically porous CuO nano-labyrinths as binder-free anodes for long-life and high-rate lithium ion batteries. Nano Energy 59(2019) 229-236.

[44] F. Pu, Y. Bai, J. Lv, X. Zhao, G. Wu, C. Kong, B. Lei, X. Zhang, H. Jin, Z. Yang, Yolk–shell Cu_2O@CuO-decorated RGO for high-performance lithium-ion battery anode, Energy Environ. Mater. 5(2022) 253-260.

[45] Z. Deng, Z. Ma, Y. Li, Y. Li, L. Chen, X. Yang, H. E. Wang, B. L. Su, Boosting Lithium-ion storage capability in CuO nanosheets via synergistic engineering of defects and pores. Front. Chem. 6(2018) 428.

[46] J. Wang, J. Wu, Z. Wu, L. Han, T. Huang, H. L. Xin, D. Wang, High-rate and long-life lithium-ion battery performance of hierarchically hollow-structured $NiCo_2O_4$/CNT nanocomposite. Electrochim. Acta 244(2017) 8-15.

[47] D. Chen, H. Tan, X. Rui, Q. Zhang, Y. Feng, H. Geng, C. Li, S. Huang, Y. Yu, Oxyvanite V_3O_5: A new intercalation-type anode for lithium-ion battery. InfoMat 1(2019) 251-259.

[48] F. Lin, D. Nordlund, T.-C. Weng, Y. Zhu, C. Ban, R. M. Richards, H. L. Xin, Phase evolution for conversion reaction electrodes in lithium-ion batteries. Nat. Commun. 5(2014) 3358.

[49] Y. Li, Y. Li, A. Pei, K. Yan, Y. Sun, C.-L. Wu, L.-M. Joubert, R. Chin, A. L. Koh, Y. Yu, et al. Atomic structure of sensitive battery materials and interfaces revealed by cryo–electron microscopy. Science 358(2017) 506-510.

[50] J. Wang, W. Huang, A. Pei, Y. Li, F. Shi, X. Yu, Y. Cui, Improving cyclability of Li metal batteries at elevated temperatures and its origin revealed by cryo-electron microscopy. Nat. Energy 4(2019) 664-670.

[51] P. F. Lindberg, S. M. Gorantla, A. E. Gunnaes, B. G. Svensson, E. V. Monakhov, Electronic properties and morphology of copper oxide/n-type silicon heterostructures. J. Phys.: Condensed Matter 29(2017) 315701.

[52] F. Wang, J. Graetz, M. S. Moreno, C. Ma, L. Wu, V. Volkov, Y. Zhu, Chemical distribution and bonding of lithium in intercalated graphite: Identification with optimized electron energy loss spectroscopy. ACS Nano 5(2011) 1190-1197.

[53] A. Débart, L. Dupont, P. Poizot, J. B. Leriche, J. M. Tarascon, A Transmission electron microscopy study of the reactivity mechanism of tailor-made CuO particles toward lithium. J. Electrochem. Soc. 148(2001) A1266.

[54] Y. Dong, X. Jiang, J. Mo, Y. Zhou, J. Zhou, Hollow CuO nanoparticles in carbon microspheres prepared from cellulose-cuprammonium solution as anode materials for Li-ion batteries. Chem. Eng. J. 381(2020) 122614.

[55] G. Evmenenko, T. T. Fister, F. C. Castro, X. Chen, B. Lee, D. B. Buchholz, V. P. Dravid, P. Fenter, M. J. Bedzyk, Structural analysis of the initial lithiation of NiO thin film electrodes. Phys. Chem. Chem. Phys. 21(2019) 8897-8905.

[56] C. Wang, R. Zhang, K. Kisslinger, and H. L. Xin, Atomic-scale observation of O1 faulted phase-induced deactivation of $LiNiO_2$ at high voltage, Nano Lett. 21(2021) 3657-3663

[57] R. D. Leapman, L. A. Grunes, P. L. Fejes, Study of the L_{23} edges in the *3d* transition metals and their oxides by electron-energy-loss spectroscopy with comparisons to theory. Phys. Rev. B 26(1982) 614-635.

[58] D. R. Lide, CRC handbook of chemistry and physics; CRC press, 2004.

[59] P. Verma, P. Maire, P. Novák, A review of the features and analyses of the solid electrolyte interphase in Li-ion batteries. Electrochim. Acta 55(2010) 6332-6341.

Figures

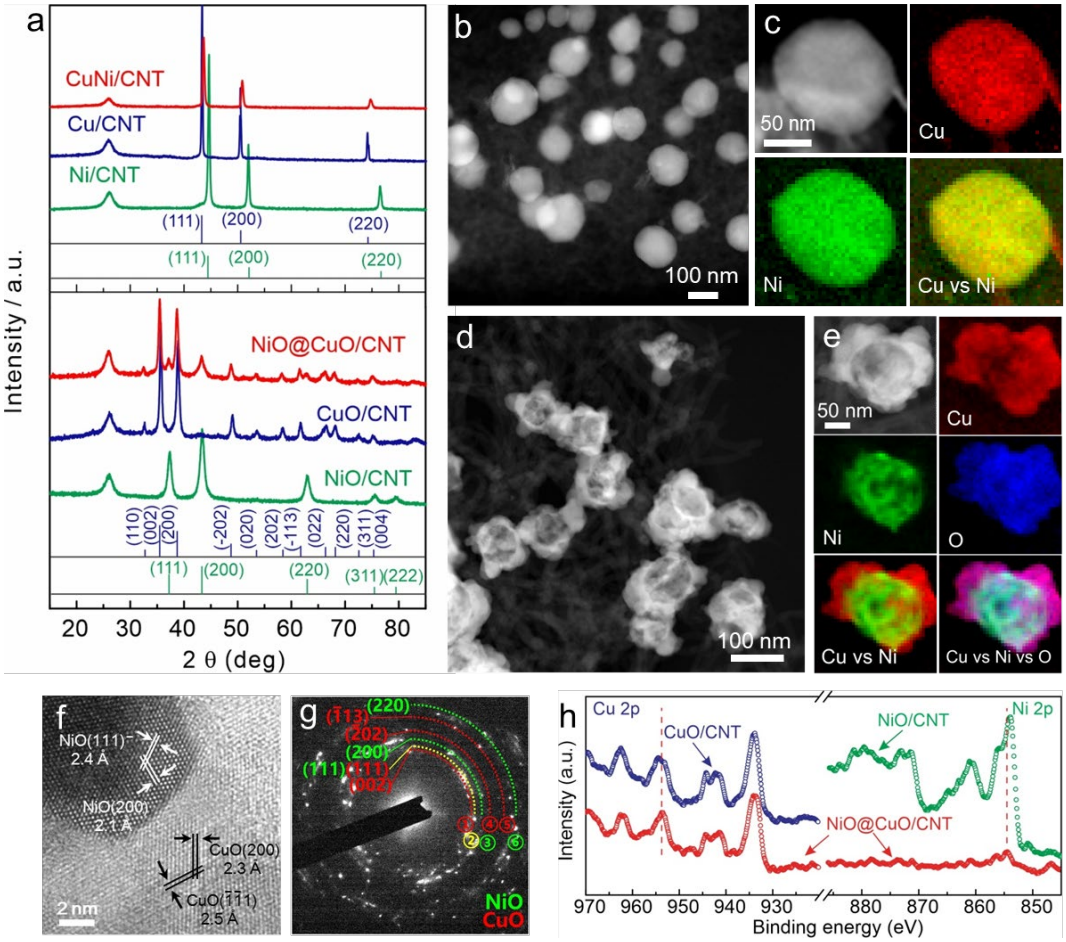

Figure 1 Morphology, structure, and composition of the pristine samples. (a) XRD spectra of NiCu alloy, Cu, Ni, NiO@CuO, CuO, and NiO supported on CNTs. (b) HAADF-STEM image and (c) EELS maps of NiCu particles. (d) HAADF-STEM image and (e) EELS maps of NiO@CuO particles. (f) HRTEM image and (g) SAED pattern of the NiO@CuO nanoparticle. (h) High-resolution XPS spectra showing Cu 2p and Ni 2p from NiO@CuO/CNT, NiO/CNT, and CuO/CNT.

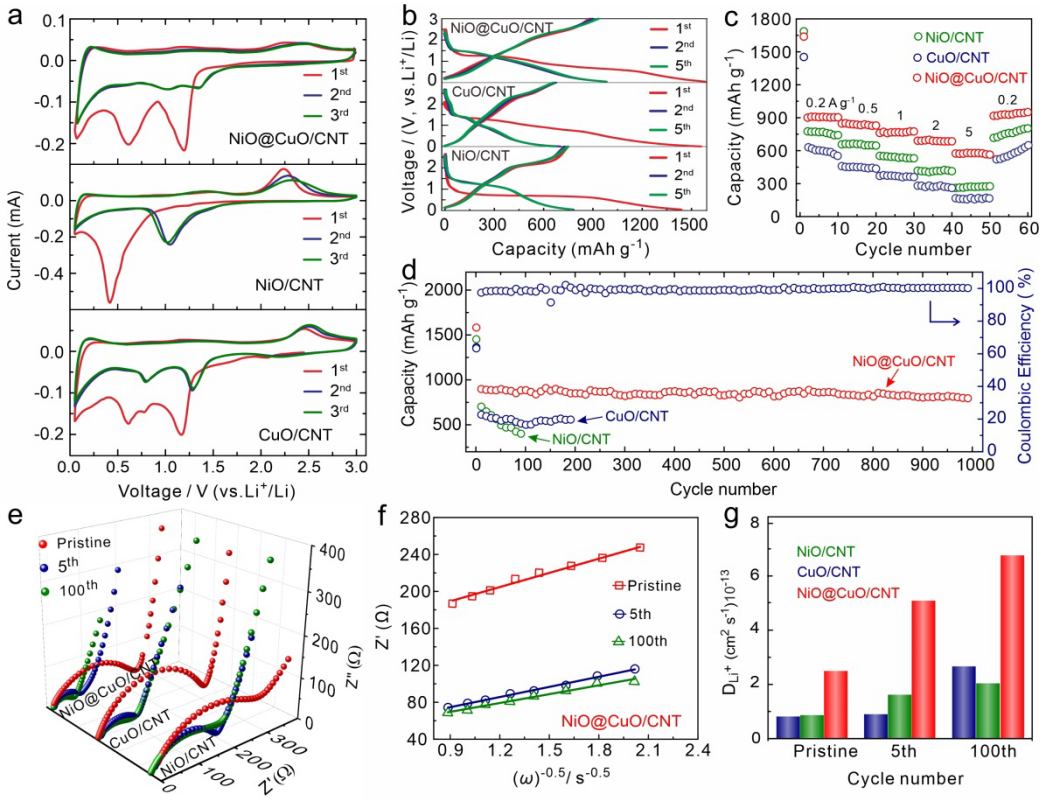

Figure 2 Electrochemical performances of NiO@CuO/CNT, NiO/CNT, and CuO/CNT. (a) CV curves of the first three cycles at a scan rate of 0.1 mV s^{-1}. (b) First five discharge-charge curves at 0.2 Ag^{-1}, (c) rate performance, (d) cycling performance at 0.5 A g^{-1}, (e) EIS spectra, (f) Z' vs. the reciprocal of the square root of frequency ($\omega^{-0.5}$) in the intermediate frequency range for NiO@CuO/CNT, and (g) histogram of D_{Li+} during different cycles.

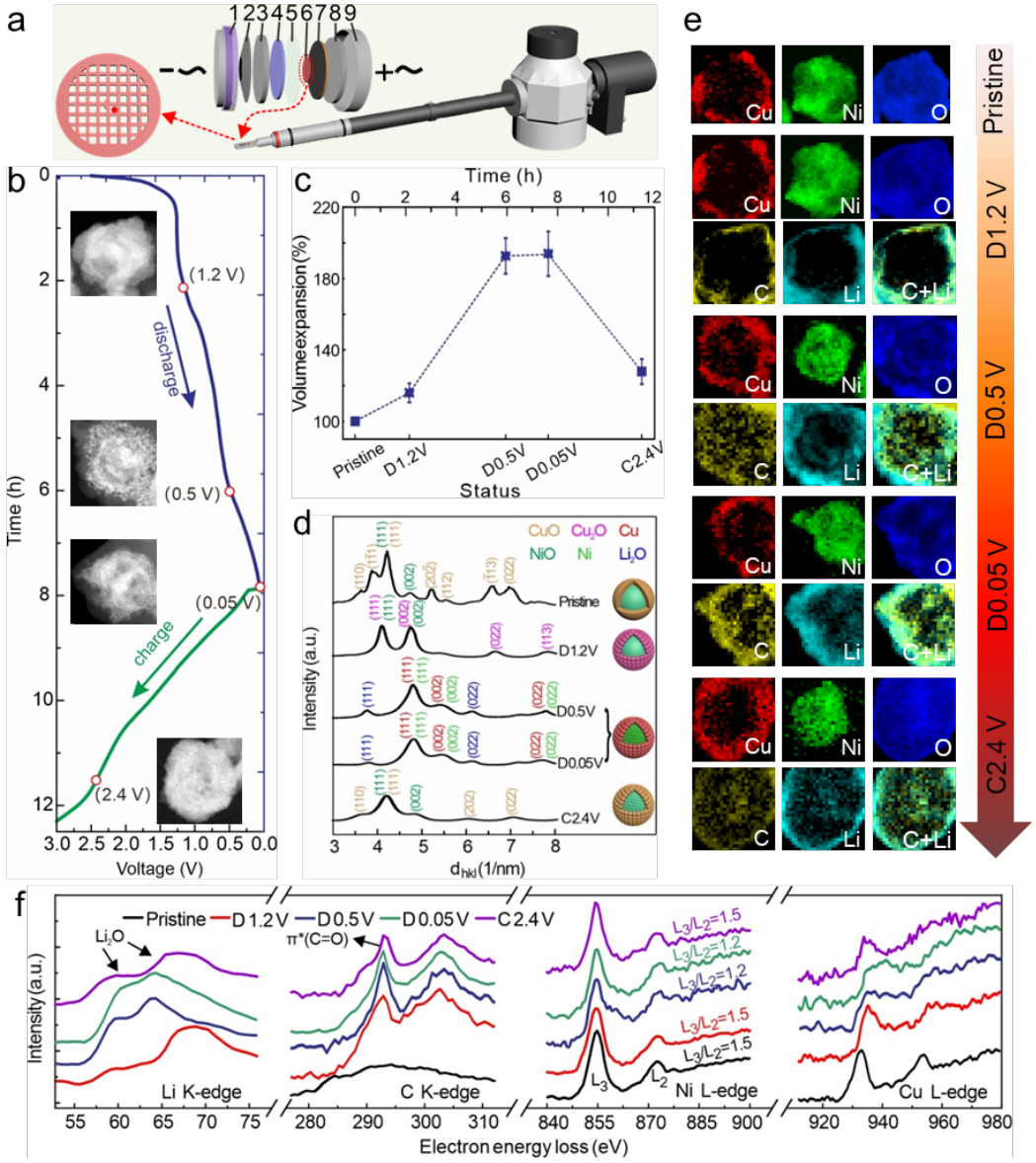

Figure 3 Identical-location *ex situ* cryo-(S)TEM examination on NiO@CuO nanoparticles at different discharge/charge states. (a) Schematic illustration of the TEM-grid-loaded coin cell design (1 bottom cap, 2 spring, 3 stainless plate, 4 lithium plate, 5 separator, 6 nanoparticle-loaded TEM grid, 7 active material on copper foil, 8 stainless plate, and 9 top cap) and cryo-TEM holder setup. (b) First discharge-charge voltage curve and the corresponding STEM images. (c) Volume expansion vs. voltage and time curve. (d) Radial-averaged SAED intensity profiles at different discharge/charge states with the schematic models on the right to illustrate the structure of NiO@CuO particles at the corresponding states. (e) EELS maps and (f) EEL spectra of NiO@CuO at different discharge/charge states.

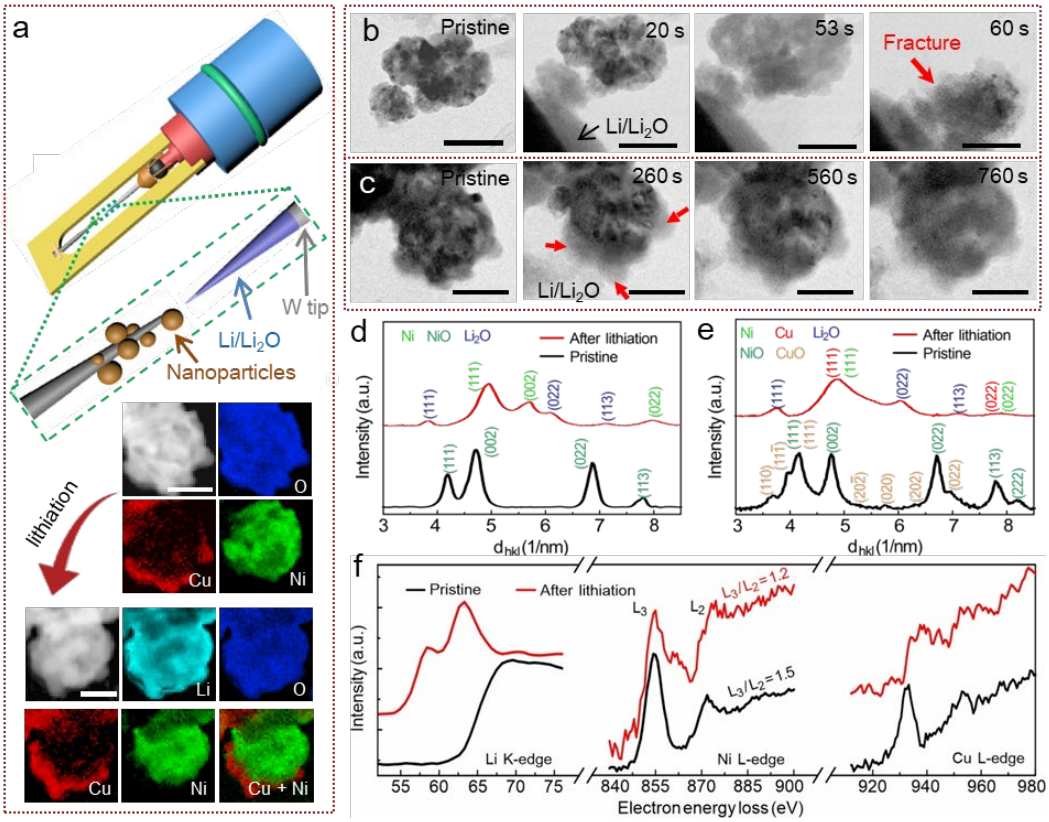

Figure 4 ***In situ*** **lithiation and TEM characterization on NiO and NiO@CuO.** (a) Schematic illustration of the holder setup for *in situ* lithiation, and HAADF-STEM images and EELS maps of a NiO@CuO particle before and after *in situ* lithiation. Time-sequenced TEM images showing the structure evolution of (b) NiO and (c) NiO@CuO nanoparticles during *in situ* lithiation. (d-f) Radial-averaged SAED intensity profiles of the (d) NiO and (e) NiO@CuO nanoparticles, and (f) EEL spectra of NiO@CuO before and after *in situ* lithiation. The scale bar is 100 nm.

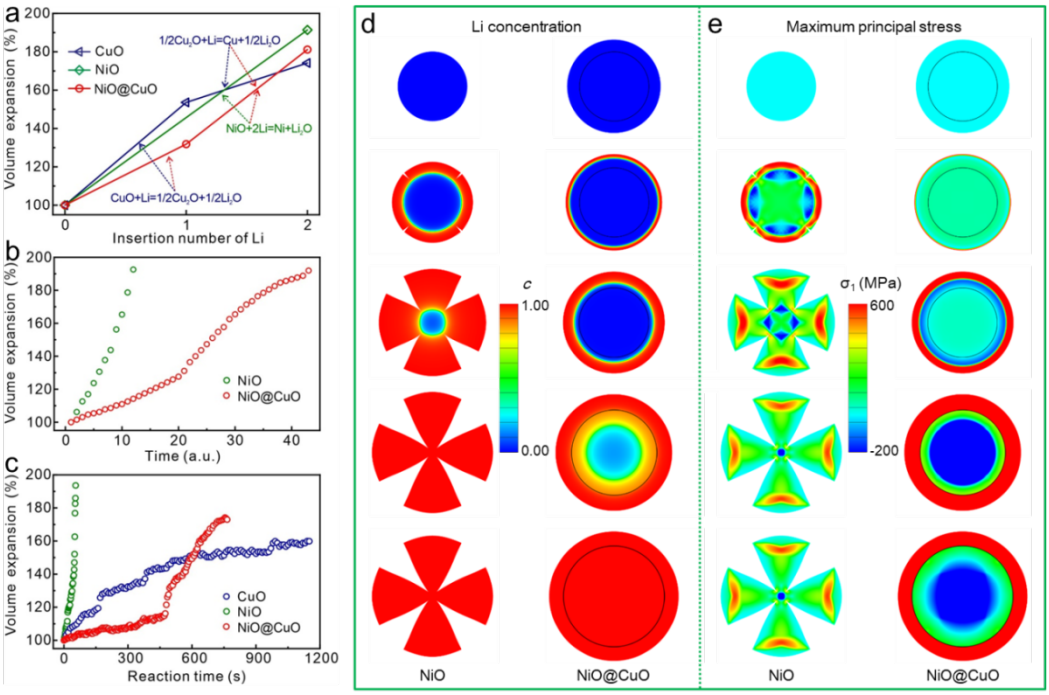

Figure 5 Comparison of volume expansion for NiO, CuO, and NiO@CuO during lithiation process. (a) Calculated unit cell volume expansion of the three nanoparticles. (b) Volume expansion pathways derived from chemomechanical simulations. (c) Volume expansion of the three particles measured from *in situ* TEM observation. (d,e) Chemomechanical simulated time-series snapshots of (d) Li concentration and (e) maximum principal stress distributions in NiO (left) and NiO@CuO (right) particles, respectively. c and σ represent the normalized Li concentration and the stress, respectively.